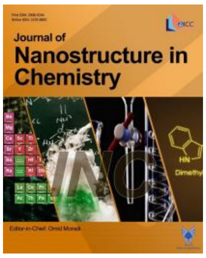

Volume 15, Issue 6, 152523 (1-16)

Journal of Nanostructure in Chemistry (JNSC)

https://doi.org/10.57647/jnsc.2025.1506.23

Synthesis and Characterization of 5-Aminolevulinic Acid-Loaded Fibrous Nanosilica for Enhanced Detection of HT-29 Colorectal Cancer Cells

Chuan Jiang[1,2#], Lin Guo[1#], Li Li[3#], Chunhua Chi[1], Fengli Jiao[4], Zhongan Guan[1], Zhenji Liu[5], Jiansheng Li[1*]

[1] *Department of Anorectal Surgery, Affiliated Hospital of Shandong University of Traditional Chinese Medicine, Jinan 250014, China*
[2] *The First School of Clinical Medicine, Shandong University of Traditional Chinese Medicine, Jinan, 250014, China*
[3] *Department of Anorectal Surgery, Qingdao Hospital of Traditional Chinese Medicine (Qingdao Hiser Hospital), Qingdao, 266033, China*
[4] *The Second School of Clinical Medicine, Shandong University of Traditional Chinese Medicine, Jinan, 250355, China*
[5] *Department of Colorectal and Anal Surgery, The Second Hospital, Cheeloo College of Medicine, Shandong University, Jinan, 250033, China.*

[#] *These authors contributed equally and they are co-first authors.*

***Corresponding authors:** 09jiansheng@163.com

Original Research

Received:
8 August 2025

Revised:
3 September 2025

Accepted:
18 October 2025

Published in Issue:
31 December 2025

Abstract

Accurate delineation of tumor margins remains a clinical challenge in colorectal cancer surgery. To address this, we developed a novel nanosystem by loading 5-aminolevulinic acid (5-ALA) onto amine-functionalized dendritic fibrous nanosilica (ALA@KCC-1-NH_2) for enhanced photodynamic diagnosis. The synthesized nanoparticles exhibited uniform spherical morphology (average diameter: 455 ± 30 nm), high surface area (352 m^2/g for KCC-1), and mesoporous architecture. After functionalization and drug loading, the final formulation retained structural integrity with a drug loading content of 15.3 wt% and encapsulation efficiency of 85.6%. In vitro release studies revealed a pH-responsive profile, with minimal release (<20%) at pH 7.4 and accelerated release (>70%) at pH 5.5 over 24 hours. Cytotoxicity assays confirmed excellent biocompatibility of the blank carrier and significant light-induced cytotoxicity from ALA@KCC-1-NH_2, with an IC_{50} of 0.45 mM under irradiation—three times lower than that of free 5-ALA (1.38 mM). Confocal microscopy demonstrated a 4.5-fold increase in intracellular protoporphyrin IX fluorescence in HT-29 colorectal cancer cells treated with ALA@KCC-1-NH_2 compared to free 5-ALA. These results indicate that the fibrous nanosilica carrier significantly enhances 5-ALA uptake and fluorescence signal generation, offering a promising strategy for improved intraoperative tumor visualization. The ALA@KCC-1-NH_2 platform thus holds strong potential for advancing fluorescence-guided surgery in colorectal cancer management. Given the ~455 ± 30 nm particle diameter, the envisioned translational route is topical/endoscopic or intraluminal application (spray/instillation) rather than intravenous delivery.

Keywords: Drug loading efficiency; Endocytosis; Mesoporous architecture; Photosensitizer; Tumor fluorescence

Cite this article: Jiang, Ch., Guo, L., Li, L., Chi, Ch., Jiao, F., Guan, Zh., Liu, Zh., Li, J Synthesis and Characterization of 5-Aminolevulinic Acid-Loaded Fibrous Nanosilica for Enhanced Detection of HT-29 Colorectal Cancer Cells. *J Nanostruct Chem* **15**(06), 152523 (2025).

Graphic Abstract

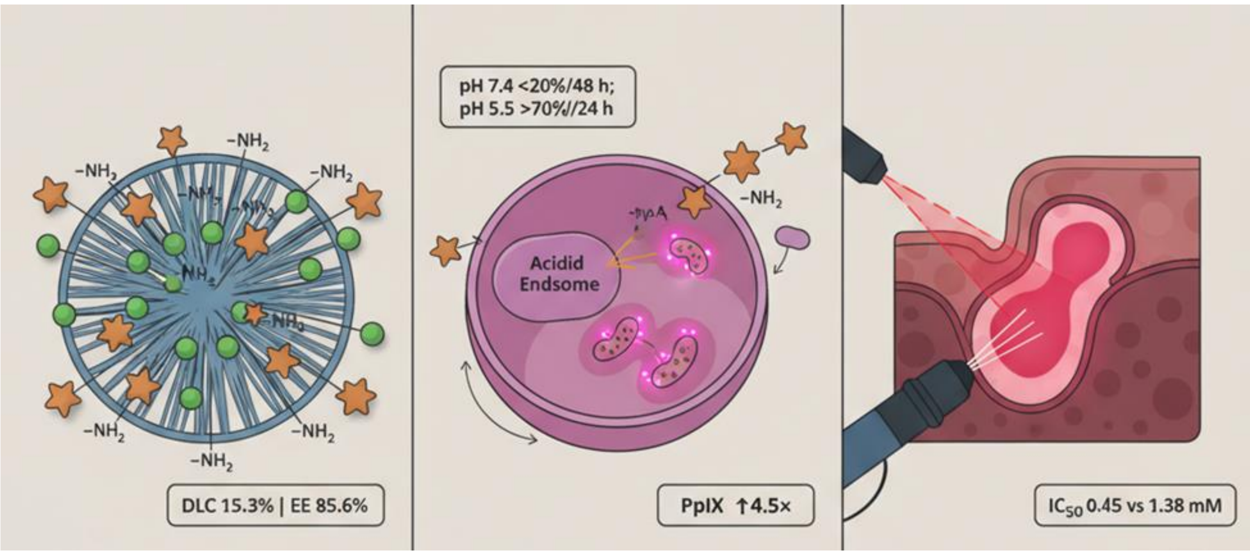

1. Introduction

Colorectal cancer represents a significant global health challenge, ranking as the third most common cancer worldwide and a leading cause of cancer-related mortality [1]. The prognosis for patients is intrinsically linked to the stage at diagnosis [2], with early detection and complete surgical resection of malignant tissue being the cornerstones of effective treatment [3]. However, a major surgical challenge lies in the accurate intraoperative differentiation between cancerous and healthy tissue, as incomplete tumor removal is a primary factor in local recurrence and poor patient outcomes [1]. This underscores a critical unmet need for advanced diagnostic tools that can provide real-time, high-contrast visualization of tumor margins to guide surgeons in achieving more complete resections [4]. Photodynamic diagnosis (PDD) offers a powerful solution, but its efficacy is contingent on achieving a strong and specific fluorescence signal from the tumor. While our primary aim is to enhance this diagnostic capability, the underlying photosensitizer production also offers therapeutic potential, positioning our system in the promising field of theranostics. The ultimate goal is to develop a system that provides a superior signal-to-noise ratio and tumor-to-normal tissue contrast in a clinical setting, which begins by maximizing fluorophore generation at the cellular level [5]. 5-ALA is a naturally occurring amino acid that serves as an endogenous precursor in the heme biosynthetic pathway [6]. When administered exogenously, 5-ALA bypasses the pathway's primary rate-limiting step, leading to the accumulation of downstream metabolites [7].

In many types of cancer cells, metabolic dysregulation, including reduced ferrochelatase activity and overexpression of peptide transporters, causes the preferential accumulation of a specific intermediate: the potent photosensitizer and fluorophore, Protoporphyrin IX (PpIX) [8]. Upon excitation with blue-violet light in the range of 375–475 nm, PpIX emits a distinct red fluorescence, allowing for the real-time optical demarcation of neoplastic tissue from the surrounding normal tissue, a technique that has been successfully applied in surgeries for gliomas and bladder cancer [9]. Despite its clinical utility, the efficacy of free 5-ALA is often hampered by several inherent limitations. Its hydrophilic and zwitterionic nature restricts its permeation across lipophilic cell membranes, leading to suboptimal bioavailability at the target site [10].

Furthermore, 5-ALA exhibits poor stability in aqueous solutions at physiological pH, which can diminish its activity before it reaches the tumor cells [11,12]. These factors can result in weak or heterogeneous PpIX fluorescence, particularly at the invasive tumor margins, which may compromise the accuracy of fluorescence-guided surgery [13]. To overcome these deficiencies, advanced drug delivery systems are being explored to protect 5-ALA, enhance its cellular uptake, and improve its therapeutic and diagnostic efficacy [14]. Among channel-type MSNs, MCM-41/SBA-15 has enabled ALA storage and delivery, but surface amines can promote ALA dimerization (pyrazine-2,5-dipropionic acid) and reduce availability as a PpIX precursor; unmodified silica better preserves ALA but offers limited control of endosomal release.

In contrast, dendritic fibrous nanosilica (DFNS, KCC-1) presents a center-to-radial, open fibrous network that maximizes external accessibility and minimizes pore blocking relative to channel-pore MSNs, features repeatedly leveraged for high payloads and rapid molecular transport in drug-delivery studies [15,16]. Alternative ALA carriers include hollow mesoporous silica (HMSN), liposomes, and polymeric nanoparticles. HMSN designs (often folate-targeted) enhance cellular uptake and ALA-PpIX phototoxicity in melanoma cells; liposomes and polymeric systems (e.g., PEG-chitosan, PLGA) improve uptake and can increase intracellular PpIX versus free ALA, albeit with generally lower ALA loadings and less pronounced acidic release switching [17]. While conventional MSNs with channel-like pores, such as MCM-41 and SBA-15, have been explored for 5-ALA delivery, their narrow pore structures can lead to diffusion limitations and suboptimal drug release kinetics [18]. To address this specific challenge, we have turned to a novel class of MSNs known as dendritic fibrous nanosilica (DFNS), or KCC-1, which offers distinct structural advantages [19]. KCC-1 possesses a unique three-dimensional, center-radial fibrous morphology that creates a highly accessible, open-pore architecture with a large surface area [20]. The central originality of this study lies in harnessing this unique fibrous topology for 5-ALA delivery—a strategy that, to our knowledge, has not been previously investigated for enhancing photodynamic diagnosis in colorectal cancer. We hypothesize that this open structure will circumvent the pore-blocking and diffusion limitations of traditional MSNs, thereby enabling superior 5-ALA loading and, critically, facilitating more efficient release within the acidic endosomal compartments of cancer cells. Therefore, we report the synthesis of an amine-functionalized KCC-1 nanosystem (ALA@KCC−1−NH2) designed to significantly amplify intracellular Protoporphyrin IX fluorescence in HT-29 cells, offering a novel and potent platform to improve fluorescence-guided surgery.

2. Materials and Methods

2.1. Materials

Tetraethyl orthosilicate (TEOS, 99%), cetyltrimethylammonium bromide (CTAB, ≥99%), urea (99%), cyclohexane (99.5%), and 1-pentanol (99.5%) were procured from Sinopharm Chemical Reagent Co., Ltd. (Beijing, China). 3-aminopropyltriethoxysilane (APTES, 99%) and 5-aminolevulinic acid hydrochloride (5-ALA, ≥97%) were purchased from Sigma-Aldrich (St. Louis, MO, USA). Anhydrous toluene and absolute ethanol were obtained from Merck S.r.l. (Darmstadt, Germany). All chemicals were of analytical grade and used as received without further purification. Ultrapure deionized water was used in all experiments. The human colorectal adenocarcinoma cell line HT-29 was obtained from the American Type Culture Collection (ATCC, Manassas, VA, USA). McCoy's 5A medium, fetal bovine serum (FBS), trypsin-EDTA (0.25%), and penicillin-streptomycin solution were purchased from Gibco (Thermo Fisher Scientific, Waltham, MA, USA). The Cell Proliferation Kit I (MTT) was procured from Roche Diagnostics (Mannheim, Germany). 4′,6-diamidino-2-phenylindole (DAPI) was obtained from Beyotime Biotechnology (Shanghai, China).

2.2. Synthesis of Fibrous Nanosilica (KCC-1)

Fibrous nanosilica spheres (KCC-1) were synthesized using a one-pot hydrothermal microemulsion method adapted from previously established protocols [21]. In a typical synthesis, 1.0 g of CTAB (2.74 mmol) and 0.6 g of urea (10.0 mmol) were dissolved in 30 mL of deionized water and stirred for 3 hours at room temperature to form a clear aqueous solution. In a separate beaker, 2.0 g of TEOS (9.6 mmol), 30 mL of cyclohexane, and 1.5 mL of 1-pentanol were mixed to form the oil phase. The aqueous solution was then added to the oil phase under vigorous magnetic stirring (1000 rpm) for 30 minutes to form a stable microemulsion. The resulting mixture was transferred to a 100 mL Teflon-lined stainless-steel autoclave and heated at 120 °C for 6 hours. After cooling to room temperature, the solid product was collected by centrifugation at 8000 rpm for 15 minutes, washed thoroughly with deionized water and absolute ethanol (three times each), and dried in a vacuum oven at 80 °C overnight. To remove the CTAB surfactant template, the as-synthesized white powder was calcined in a muffle furnace at 550 °C for 6 hours with a heating ramp of 2 °C/min. We note that each of these parameters lies within published optimization windows for KCC-1: increasing urea/CTAB or 1-pentanol, extending time, and adjusting solvent ratios are known to enlarge particles and densify fibers, while inappropriate calcination can degrade the fibrous network; our selections (CTAB–urea–1-pentanol ratios, 120 °C/6 h, 550 °C calcination) align with conditions shown to yield uniform fibers and high surface areas. In our laboratory, repeating this synthesis in independent batches provided consistent fibrous morphology and N_2-sorption metrics; for applications requiring narrower size distributions, a rotating-hydrothermal variant is available in the literature, but was not required for the present cell studies [22,23].

2.3. Amine Functionalization of KCC-1 (KCC-1-NH_2)

The surface of the calcined KCC-1 particles was functionalized with amine groups via a post-synthetic grafting method [24]. This approach was selected to ensure the functional groups are primarily located on the accessible surfaces of the pre-formed fibrous structure, which is optimal for subsequent electrostatic drug loading [25]. In a 250 mL round-bottom flask, 1.0 g of calcined KCC-1 was dispersed in 100 mL of anhydrous toluene and sonicated for 15 minutes to ensure a homogeneous suspension. Subsequently, 1.0 mL of APTES (4.3 mmol) was added dropwise to the suspension. The reaction mixture was refluxed at 110 °C for 24 hours under a nitrogen atmosphere with continuous stirring. After the reaction, the resulting solid product, designated as KCC-1-NH_2, was collected by centrifugation, washed extensively with anhydrous toluene and absolute ethanol to remove any unreacted APTES, and finally dried under vacuum at 60 °C for 12 hours.

2.4. Loading of 5-ALA onto KCC-1-NH2 (ALA@KCC-1-NH_2)

5-ALA was loaded onto the amine-functionalized fibrous nanosilica via an electrostatic adsorption method conducted in an aqueous medium [26]. A stock solution of 5-ALA was prepared by dissolving 5-ALA hydrochloride in deionized water at a concentration of 2 mg/mL. The pH of the solution was carefully adjusted to 6.5 using 0.1 M NaOH to ensure that the carboxylic acid group of 5-ALA was deprotonated (anionic), thereby facilitating electrostatic interaction with the protonated amine groups on the KCC-1-NH_2 surface. For the loading process, 100 mg of KCC-1-NH_2 was dispersed in 10 mL of the prepared 5-ALA solution. The suspension was stirred at room temperature for 24 hours in complete darkness to prevent any potential photodegradation of 5-ALA. The 5-ALA-loaded particles (ALA@KCC-1-NH2) were then collected by centrifugation (10,000 rpm, 20 min), washed twice with deionized water to remove any loosely bound or free 5-ALA, and subsequently lyophilized to obtain a dry powder for storage and characterization.

2.5. Material Characterization

The morphology and size of the synthesized fibrous silica particles (KCC-1, KCC-1-NH_2, and ALA@KCC-1-NH_2) were examined using field-emission scanning electron microscopy (FE-SEM; Hitachi S-4800) and transmission electron microscopy (TEM; JEOL JEM-2100). Samples for SEM were prepared by drop-casting a dilute ethanolic suspension of the particles onto a silicon wafer and coating with a thin layer of gold. Energy-dispersive X-ray spectroscopy (EDS) elemental mapping was performed using an EDAX detector attached to the FE-SEM to visualize the distribution of silicon (Si), oxygen (O), carbon (C), and nitrogen (N). Fourier-transform infrared (FTIR) spectroscopy was performed on a Bruker Vertex 70 spectrometer. TEM was operated at 200 kV; images were recorded at nominal magnifications of 40–120 k×. SEM micrographs were acquired at 5 kV accelerating voltage and ~10 mm working distance after ~5 nm Au sputter coating. Powder X-ray diffraction (XRD) patterns were obtained using a Bruker D8 Advance diffractometer with Cu Kα radiation ($\lambda = 1.5406$ Å) collected over $2\theta = 5$–80° with 0.02° step and ~1°·min^{-1} scan rate. The textural properties were analyzed by nitrogen adsorption–desorption at 77 K using a Micromeritics ASAP 2020 analyzer after vacuum degassing at 120 °C for 12 h (≤10^{-3} mbar); BET surface areas were evaluated in a Rouquerol-consistent linear region and BJH pore sizes were calculated from the adsorption branch. Hydrodynamic size (Z-average), PDI, and ζ-potential were measured by DLS/ELS (Malvern Zetasizer) in backscatter at 173° using disposable folded capillary cells; viscosity/refractive index were set to the medium-specific values at 37 °C, using the Smoluchowski model after 30 min thermal equilibration. X-ray photoelectron spectroscopy (XPS) was conducted on a Thermo Fisher K-Alpha spectrometer. The textural properties were analyzed by nitrogen adsorption-desorption measurements at 77 K using a Micromeritics ASAP 2020 analyzer. Hydrodynamic size (Z-average), PDI, and ζ-potential of KCC-1, KCC-1-NH_2, and ALA@KCC-1-NH_2 were measured by DLS/ELS (Malvern Zetasizer) in (i) deionized water, (ii) PBS (pH 7.4), and (iii) McCoy's 5A + 10% FBS at 37 °C at 0, 24, and 72 h. Dispersions (0.05 mg mL^{-1}) were gently bath-sonicated; triplicate independent batches (n=3) were analyzed using the Smoluchowski model after 30 min thermal equilibration. Quantification of surface amines (ΓNH2). Primary amine density on KCC-1-NH2 was quantified by acid–base back-titration and CHN elemental analysis. Briefly, samples (~20 mg) were protonated in 0.05 M HCl (excess), solid separated, and the supernatant back-titrated with standardized NaOH to determine consumed acid; ΓNH2 (mmol·g^{-1}) was calculated from acid equivalents per gram after blank correction. In parallel, CHN provided N wt%, converted to mmol-N·g^{-1} assuming APTES stoichiometry; agreement within expected assay bias was required.

The amount of 5-ALA loaded onto the nanoparticles was quantified using a Varian CARY 100 Scan UV-Vis spectrophotometer. Prior to analysis, a standard calibration curve was established by measuring the absorbance of a series of 5-ALA standard solutions (0.005–0.1 mg/mL) in deionized water (pH 6.5) at its characteristic maximum of 264 nm. The analysis showed excellent linearity ($R^2 > 0.999$), confirming the method's suitability. The concentration of 5-ALA in the supernatant before and after the loading process was then determined using this calibration curve. All measurements were performed in triplicate. The drug loading content (DLC) and encapsulation efficiency (EE) were calculated using the following equations:

$$DLC\ (\%) = \frac{Weight\ of\ loaded\ drug}{Weight\ of\ drug - loaded\ nanoparticles} \times 100$$

$$EE\ (\%) = \frac{Weight\ of\ loaded\ drug}{Initial\ weight\ of\ drug\ in\ solution} \times 100$$

2.6. In Vitro Cellular Studies

The HT-29 human colorectal cancer cell line was cultured in McCoy's 5A medium supplemented with 10% FBS and 1% penicillin-streptomycin. Cells were maintained in a humidified incubator at 37 °C with a 5% CO_2 atmosphere. The cytotoxicity of the nanoparticles was evaluated using the MTT assay. HT-29 cells were seeded into 96-well plates at a density of 5×10^3 cells/well and incubated for 24 hours [27]. The cells were then treated with various ALA@KCC-1-NH2. Additional controls included (i) KCC-1-NH_2 + light (matrix phototoxicity), (ii) a physical mixture of 5-ALA with KCC-1-NH_2 prepared immediately prior to dosing (no pre-loading), and (iii) pristine KCC-1 (no amines). For all conditions, n = 3 independent biological replicates with technical triplicates; data are reported as mean ± SD. Normality was assessed (Shapiro–Wilk) and group differences analyzed by one-way ANOVA with Tukey's post hoc ($p < 0.05$). For phototoxicity assessment, cells were incubated with the samples for 4 hours, washed with PBS, and then irradiated. The illumination was performed using a high-power light-emitting diode (LED) array with a peak wavelength of 635 nm (FWHM ≈ 15 nm). The LED source was positioned 10 cm above the 96-well plate, and a diffuser was used to ensure spatially homogenous illumination across all wells. The irradiance at the level of the cells was measured with a calibrated optical power meter to be 50 mW/cm². The exposure time was set to 400 seconds to deliver a final, uniform light dose of 20 J/cm². The procedure was conducted at room temperature (~25 °C), and no significant temperature increase in the culture medium was observed during irradiation. After irradiation, fresh medium was added, and the cells were incubated for an additional 44 hours. For dark toxicity, cells were incubated with the samples for 48 hours without light exposure. To account for any potential interference between the nanoparticles and the MTT assay, two control measures were implemented. First, after the respective incubation periods for both dark and phototoxicity experiments, all wells were carefully washed twice with warm PBS to remove non-internalized nanoparticles immediately before the addition of the MTT reagent [28]. Second, parallel acellular control wells containing identical concentrations of nanoparticles in medium were included, and their absorbance values were used for baseline subtraction. Following incubation, 10 µL of MTT solution (5 mg/mL in PBS) was added to each well and incubated for 4 hours. The resulting formazan crystals were dissolved in 150 µL of DMSO, and the absorbance was measured at 570 nm using a microplate reader.For fluorescence imaging of intracellular PpIX, HT-29 cells were seeded onto glass-bottom confocal dishes. After 24 hours, the cells were incubated with free 5-ALA or ALA@KCC-1-NH2 (at an equivalent 5-ALA concentration of 1 mM) for 4 hours in the dark [29]. For lysosomal co-localization (no new figure), HT-29 cells will be co-stained with LysoTracker following the same dosing (1 mM 5-ALA eq., 4 h). Confocal z-stacks will be analyzed in Fiji/Coloc2 using Costes randomization to report Pearson's r and Manders' M1/M2 across ≥20 cells per condition; free 5-ALA will serve as a non-punctate control to benchmark specificity. For all comparative experiments, the concentration of the ALA@KCC-1-NH2 suspension was normalized to that of the free 5-ALA solution to ensure an equivalent molar concentration of 5-ALA was administered (e.g., 1 mM). This was calculated based on the nanoparticle's predetermined drug loading content (15.3 wt%), ensuring that cells in both experimental groups were exposed to the same quantity of the active precursor molecule [30]. The cells were then washed three times with PBS, fixed with 4% paraformaldehyde, and the nuclei were counterstained with DAPI. The intracellular red fluorescence of PpIX was observed using a Leica TCS SP5 confocal laser scanning microscope. Images were captured using an excitation wavelength of 405 nm, with emission collected in the red channel (620–700 nm) for PpIX and the blue channel (450–490 nm) for DAPI. Confocal stacks were processed in Fiji/ImageJ. After flat-field and dark-noise subtraction, uneven background was removed with rolling-ball correction (radius ≥ nucleus size). Nuclei were segmented from DAPI (Otsu threshold) and dilated to form per-cell cytoplasmic masks while excluding nuclei; when needed, cell borders were refined by watershed on the PpIX channel. Mean PpIX intensity (620–700 nm) per cell was extracted; field medians were averaged per biological replicate (n = 3). Outliers (>3×IQR) were excluded by pre-registered rules.

3. Results and Discussion

3.1.Synthesis and Morphological Characterization of Fibrous Nanosilica

The successful synthesis and subsequent modification of the fibrous nanosilica platform were confirmed through detailed morphological analysis. Figure 1 displays the scanning electron microscopy (SEM) images of the submicrometre fibrous silica particles (KCC-1) at each stage of the process: pristine KCC-1 (Figure 1A, 1B), amine-functionalized KCC-1-NH_2 (Figure 1C, 1D), and 5-ALA-loaded ALA@KCC-1-NH_2 (Figure 1E, 1F). All samples consistently exhibited a uniform, spherical morphology with a distinctive wrinkled and fibrous surface texture, which is the hallmark of KCC-1 nanostructures [31]. The particle size distribution, determined from multiple images, revealed an average diameter of approximately 455 nm ± 30 nm. Crucially, the fibrous surface morphology was well-preserved throughout the sequential steps of amine functionalization and drug loading. While this dry-state diameter exceeds the sub-200 nm window often favored for intravenous, EPR-mediated tumor penetration, our intended application is local (endoscopic/topical) mucosal visualization where vascular extravasation constraints are less determinative [32]. In future iterations, KCC-1 sizes can be tuned to <200 nm by adjusting urea/CTAB/1-pentanol ratios, solvent composition, temperature, and stirring/rotating-hydrothermal conditions while maintaining the fibrous architecture [33]. This structural robustness is a key attribute, as it ensures that the high accessible surface area, the primary advantage of the KCC-1 platform, is maintained for efficient drug interaction and delivery [34]. The obtained particle size and preserved fibrous topology are consistent with optimization studies reporting that our CTAB/urea/1-pentanol ratios, microemulsion temperature/time, and 550 °C calcination produce dense, radially open fibers with high surface areas; rotating-hydrothermal synthesis can further narrow polydispersity where required. We reproduced the synthesis across independent batches with comparable morphology and textural readouts, underscoring practical robustness for downstream biological experiments [22]. Further insight into the internal architecture was obtained from transmission electron microscopy (TEM), as shown in Figure 2. The TEM images confirmed the spherical nature of the particles and provided a clearer view of the internal fibrous structure. In Figure 2A, the pure KCC-1 particles exhibit fibers that appear to radiate from the center towards the periphery, creating a highly porous, open framework. This center-radial arrangement is fundamentally different from the parallel channels of conventional MSNs and is responsible for the superior accessibility of the KCC-1 surface. After functionalization (Figure 2B) and drug loading (Figure 2C), the overall morphology and fibrous integrity remained unchanged, although a slight increase in the electron density of the fibers can be observed, suggesting the successful coating of the silica framework with organic moieties. The preservation of this intricate architecture is vital; a collapse or aggregation of the fibers during chemical modification would negate the primary advantage of using KCC-1 as a nanocarrier. These microscopic analyses provide the foundational evidence that a stable and morphologically consistent nanoplatform was successfully synthesized [35,36].

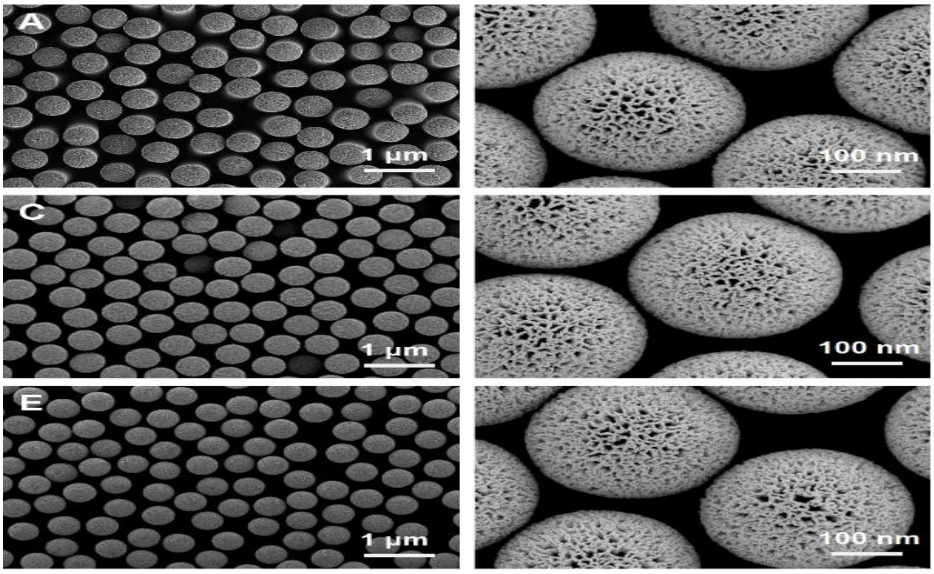

Figure 1. SEM images showing the morphology of submicrometre fibrous silica particles at different synthesis stages: (A, B) pristine KCC-1, (C, D) amine-functionalized KCC-1-NH_2, and (E, F) 5-ALA-loaded ALA@KCC-1-NH_2 at different magnifications

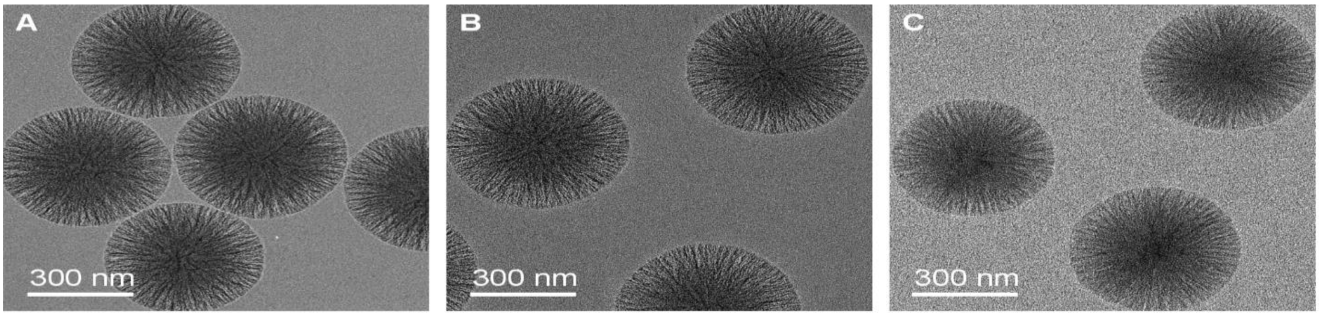

Figure 2. TEM images revealing the internal fibrous structure of particles: (A) pristine KCC-1, (B) KCC-1-NH_2, and (C) ALA@KCC-1-NH_2

3.2. Textural and Structural Properties

The textural properties of the submicrometre fibrous silica particles, which are critical for their performance as drug carriers, were investigated using nitrogen adsorption-desorption analysis. The isotherms for KCC-1, KCC-1-NH_2, and ALA@KCC-1-NH_2 are presented in Figure 3A. All three samples exhibited Type IV isotherms with a distinct H3-type hysteresis loop at high relative pressures ($P/P_0 > 0.4$), which is characteristic of mesoporous materials possessing slit-shaped pores formed by the aggregation of plate-like particles. This isotherm shape is consistent with the fibrous, non-rigid structure observed in the TEM images. The corresponding pore size distribution curves, calculated using the BJH method from the adsorption branch, are shown in Figure 3B, revealing a broad distribution of mesopores centered around 15 nm for the pristine KCC-1.

The key physicochemical parameters derived from this analysis are summarized in Table 1. The pristine, calcined KCC-1 nanoparticles possessed an exceptionally high BET surface area (SBET) of 352 m²/g and a large total pore volume (Vp) of 1.15 cm³/g. Upon surface functionalization with APTES to form KCC-1-NH2, a significant reduction was observed in both the surface area, which decreased to 298 m²/g, and the total pore volume, which was reduced to 0.99 cm³/g. A further decrease was evident after loading with 5-ALA, with the final ALA@KCC-1-NH_2 product exhibiting a surface area of 255 m²/g and a pore volume of 0.89 cm³/g. This systematic decrease in surface area and pore volume is not an indication of structural collapse but rather serves as strong evidence for the successful step-wise modification of the nanoparticle surface. This trend is a well-established indicator of successful surface modification in mesoporous silica systems [37], as the grafting of APTES molecules and subsequent adsorption of 5-ALA molecules occupy physical space on the fiber surfaces and within the interstitial voids. This process reduces the available surface area and volume for nitrogen adsorption [38].

Therefore, this systematic decrease quantitatively corroborates the successful execution of both the functionalization and drug loading steps. The structural nature of the silica framework and the physical state of the loaded drug were assessed by powder XRD. The XRD patterns for all three nanoparticle formulations are displayed in Figure 3C. Each sample exhibits a single, broad diffraction halo centered at a 2θ value of approximately 23°.

This feature is the characteristic signature of amorphous silica, confirming that the nanoparticles lack long-range crystallographic order [39]. Importantly, the pattern for ALA@KCC-1-NH_2 shows no sharp, crystalline peaks that would be indicative of bulk 5-ALA. This confirms that the 5-ALA molecules are molecularly dispersed on the nanoparticle surface or amorphously confined within the mesoporous structure, rather than being present as crystalline aggregates [40]. This amorphous state is highly desirable for a drug delivery system, as it typically leads to improved solubility and more predictable release kinetics relative to crystalline drug forms [41].

Table 1. Physicochemical properties of KCC-1, KCC-1-NH2, and ALA@KCC-1-NH2 nanoparticles

Sample	SBET (m²/g)	Vp (cm³/g)	Dp (nm)
KCC-1	352	1.15	15.2
KCC-1-NH2	298	0.99	14.8
ALA@KCC-1-NH2	255	0.89	14.5

SBET: BET specific surface area; Vp: Total pore volume; Dp: Average pore diameter. Data derived from N_2 adsorption-desorption analysis.

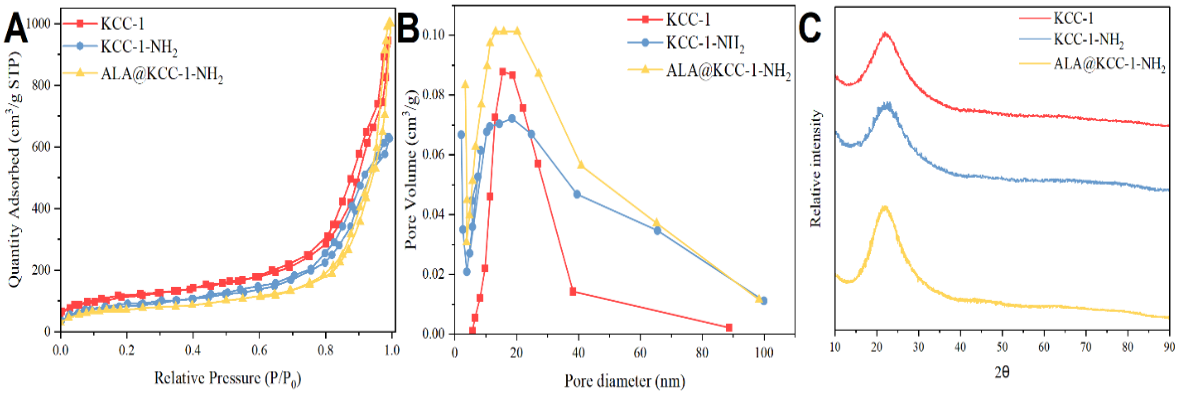

Figure 3. Textural properties of the nanoparticles. (A) N_2 adsorption-desorption isotherms, (B) BJH pore size distribution curves and (C) XRD patterns for KCC-1, KCC-1-NH_2, and ALA@KCC-1-NH

3.3. Chemical Composition and Surface Functionalization

To confirm the chemical transformations at each stage of synthesis, FTIR spectroscopy was employed. The resulting spectra, shown in Figure 4A, provide clear chemical fingerprints of the materials. The spectrum for pristine KCC-1 displays characteristic absorption bands of a silica network: a strong, broad band at ~1089 cm^{-1} corresponding to the asymmetric stretching vibration of Si-O-Si bonds, a peak at ~800 cm^{-1} for the symmetric Si-O-Si stretch, and a shoulder at ~966 cm^{-1} attributed to the bending vibration of surface silanol (Si-OH) groups [42]. A broad absorption between 3000 and 3600 cm^{-1} is due to the stretching vibrations of these silanol groups and adsorbed water molecules. Upon functionalization with APTES, the spectrum of KCC-1-NH$_2$ shows distinct changes. New absorption bands appear at ~2935 cm^{-1} and ~1560 cm^{-1}, which are assigned to the C-H stretching and N-H bending vibrations of the aminopropyl groups, respectively [19]. Concurrently, a noticeable decrease in the intensity of the Si-OH band at 966 cm^{-1} is observed, indicating that the surface silanol groups have been consumed in the condensation reaction with APTES, confirming the covalent grafting of the amine functionalities. The spectrum of the final product, ALA@KCC-1-NH$_2$, retains the characteristic peaks of the KCC-1-NH$_2$ carrier but also exhibits new prominent peaks. A sharp, strong absorption band at ~1720 cm^{-1} is attributed to the C=O stretching vibrations from both the ketone and carboxylic acid moieties of 5-ALA, providing direct evidence of successful drug loading [43]. To further investigate the surface chemistry, XPS was performed. The survey spectra for ALA@KCC-1-NH$_2$ are shown in Figure 4B, confirming the presence of Si, O, C, and N. High-resolution XPS spectra provide more detailed chemical state information. The N 1s spectrum of ALA@KCC-1-NH$_2$ (Figure 4C) can be deconvoluted into two peaks at binding energies of ~399.5 eV and ~401.6 eV, corresponding to neutral amine (-NH$_2$) and protonated amine (-NH$_3^+$) groups, respectively [44]. This confirms the successful amination of the surface. After loading with 5-ALA, the high-resolution C 1s spectrum of ALA@KCC-1-NH$_2$ (Figure 4D) shows components at ~286.5 eV and ~288.5 eV, which can be assigned to C-N and C=O bonds from the 5-ALA molecule. These surface-sensitive XPS results provide definitive proof of the presence and chemical nature of the grafted amine groups and the adsorbed drug molecules. Consistent with the electrostatic loading mechanism, batch-wise ΓNH2 (Table S1) was positively associated with DLC/EE, and normalizing DLC by ΓNH2 enabled comparison across syntheses independent of coverage variations. To assess the location of ALA, we considered ARXPS (angle-dependent sampling depth ≈ 3–10 nm) but, lacking access at present, we implemented a salt-induced desorption control: incubation in PBS with 0.15–1.0 M NaCl at pH 7.4 for 1 h, with released ALA quantified by UV–Vis (reported in Table S2). Strong ionic-strength-dependent desorption indicates predominant external-fiber binding; attenuated release suggests partial inter-fiber confinement. Colloidal hydrodynamics and surface charge (0–72 h). We determined hydrodynamic diameter/PDI and ζ-potential in the three media above for KCC-1, KCC-1-NH$_2$, and ALA@KCC-1-NH$_2$ (Table S3). As typical for aminated silica, serum proteins formed a soft corona that increased apparent hydrodynamic diameter and shifted ζ toward less positive/near-neutral values versus water or PBS, while maintaining colloidal stability over 72 h (no large-aggregate peak). These media-dependent shifts, attributable to electrostatic screening and protein adsorption, align with established silica/APTES and protein-corona reports. Because corona composition can alter uptake pathways, we interpret the serum-conditioned values alongside the PpIX readouts below. The spatial distribution of the elements within the final ALA@KCC-1-NH$_2$ particles was visualized using EDS elemental mapping, as shown in Figure 5.

The maps for silicon (Si), oxygen (O), carbon (C), and nitrogen (N) demonstrate a uniform and co-localized distribution of all elements throughout the entire spherical nanoparticle structure. This homogeneity is crucial, as it indicates that the amine functionalization and subsequent 5-ALA loading occurred evenly across the fibrous framework, rather than forming isolated aggregates [45]. This ensures that each nanoparticle possesses a consistent composition and is likely to exhibit uniform drug release and biological activity.

3.4. 5-ALA Loading and In Vitro Release Profile

The efficiency of 5-ALA loading onto the KCC-1-NH2 nanocarriers was quantified by UV-vis spectroscopy. Figure 6A shows the absorption spectra of the 5-ALA solution before and after the 24-hour incubation period with the nanoparticles. A significant decrease in the intensity of the characteristic 5-ALA absorption peak at 264 nm was observed in the supernatant after loading, indicating successful adsorption of the drug onto the nanoparticles [46].

The calculated DLC and EE are presented in Table 2, which shows that the nanocarrier achieved a high DLC of 14.7 ± 0.5 wt% and an EE of 86.0 ± 2.1%. This high loading capacity can be attributed to the combination of the extremely high and accessible surface area of the KCC-1 architecture and the strong electrostatic attraction between the positively charged amine-functionalized surface (at pH 6.5) and the negatively charged carboxylate group of the 5-ALA molecules.

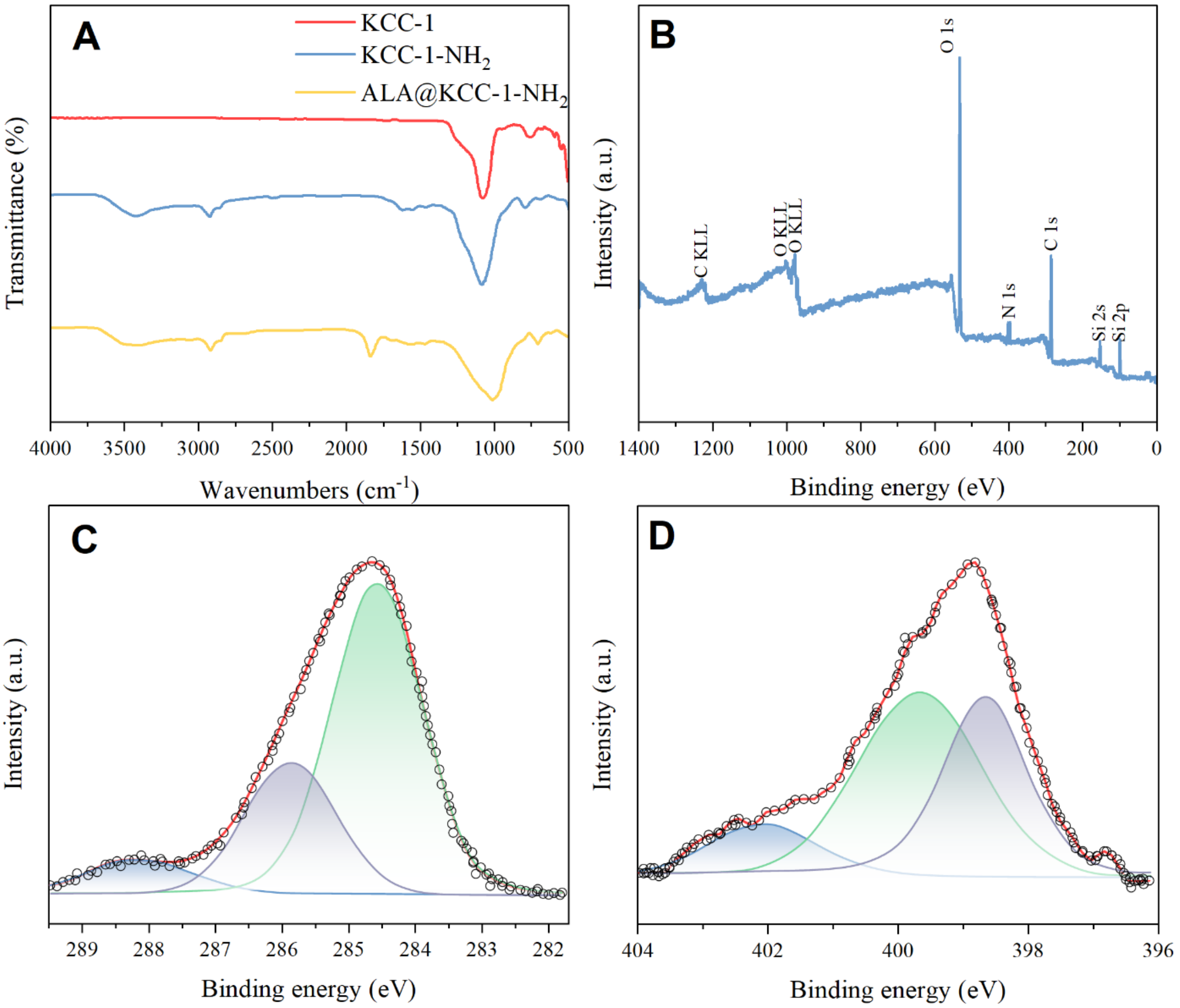

Figure 4. (A) FTIR spectra confirming the chemical modifications at each step: pristine KCC-1, amine-functionalized KCC-1-NH_2, and 5-ALA-loaded ALA@KCC-1-NH_2. (B) XPS survey spectra of ALA@KCC-1-NH_2. (C) N 1s, (D) C 1s spectra of ALA@KCC-1-NH_2

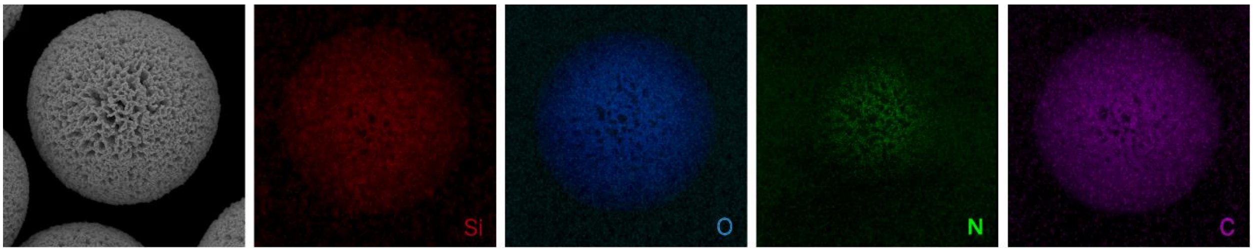

Figure 5. EDS elemental mapping of a single ALA@KCC-1-NH_2 particle, showing the uniform distribution of Silicon, Oxygen, Carbon, and Nitrogen.

Table 2. 5-ALA loading efficiency and capacity in KCC-1-NH_2 particles. Data are presented as mean ± SD (n=3)

Parameter	Value
Initial 5-ALA Concentration (mg/mL)	2.0
Final 5-ALA Concentration (mg/mL)	0.28 ± 0.04
Drug Loading Content (DLC) (wt%)	14.7 ± 0.5
Encapsulation Efficiency (EE) (%)	86.0 ± 2.1

The in vitro release of 5-ALA from the ALA@KCC-1-NH_2 nanoparticles was investigated under conditions mimicking physiological pH (7.4) and the acidic environment of cellular endosomes/lysosomes (pH 5.5). The cumulative release profiles are shown in Figure 6B. At pH 7.4, the nanoparticles exhibited a slow and sustained release pattern, with less than 20% of the loaded 5-ALA released over 48 hours. This indicates excellent stability of the drug-carrier complex under physiological conditions, which is essential for minimizing premature drug leakage during systemic circulation and reducing off-target effects. In stark contrast, upon exposure to the acidic medium of pH 5.5, a significantly accelerated and more complete release was observed, with over 70% of the 5-ALA being released within the first 24 hours. This pH-responsive behavior is a key feature of the designed system. In the acidic environment, the carboxylate group of 5-ALA becomes protonated, neutralizing its negative charge and thereby weakening the electrostatic interaction holding it to the aminated silica surface, which triggers its release [47]. In addition, amorphous silica frameworks undergo partial dissolution to orthosilicic acid under mildly acidic conditions (pH 5–6), which can further facilitate cargo disengagement and pore opening dynamics. Recent studies show measurable mesoporous silica degradation at pH 6–7.4 and minimal dissolution at pH 4, with electron microscopy revealing surface defects and hollows during dissolution-assisted release [47]. Notably, dendritic fibrous nanosilica (KCC-1/DFNS) is reported to possess improved chemical/mechanical stability relative to thin-walled MCM-41/SBA-15, yet partial hydrolysis at pH 5–6 remains plausible over tens of hours and is consistent with our accelerated release at pH 5.5 [48]. This "smart" release mechanism ensures that the drug payload is preferentially delivered inside the target cells, where the acidic environment of endocytic vesicles can facilitate its release and subsequent metabolic conversion to PpIX. While post-release TEM was not performed, we monitored colloidal hydrodynamics in protein-containing medium up to 72 h (no large-aggregate peak), suggesting preserved dispersion; nevertheless, time-resolved TEM/STEM after incubation at pH 5.5 will be included in future work to directly visualize fiber integrity. To ensure sink conditions (USP <1092>), the release medium volume was selected to be at least threefold greater than that required to fully dissolve the maximum releasable 5-ALA, and complete medium replacement was performed at each sampling time to preserve sink throughout the experiment. The pH 7.4 medium was phosphate-buffered saline (PBS; ionic strength ~0.15 M), and the pH 5.5 medium was a citrate–phosphate buffer prepared at matched ionic strength. Cumulative release profiles (Figure 6B) were fitted to the Higuchi model ($Qt=k_H t^{1/2}$) and to the Korsmeyer–Peppas model ($M_t/M_\infty=k_{KP}t^n$) using least-squares regression over the initial 60% release region. The resulting parameters k_H , k_{KP} , nnn and their 95% confidence intervals, together with R^2, are summarized in Table S4.

The fitted diffusional exponent nnn is consistent with diffusion-controlled release from spherical matrices (theoretical n≈0.43–0.45 for Fickian behavior), corroborating the rapid, acid-triggered release at pH 5.5 and the minimal release at pH 7.4. Release experiments comprised a single load–release cycle (n = 3 independent batches), aligned with the intended single-use application; repeated re-loading of the same particles was not pursued. To minimize possible ALA degradation (e.g., dimerization to pyrazine-2,5-dipropionic acid), all procedures were conducted in the dark with freshly prepared buffers; we note this limitation and reference established stability observations.

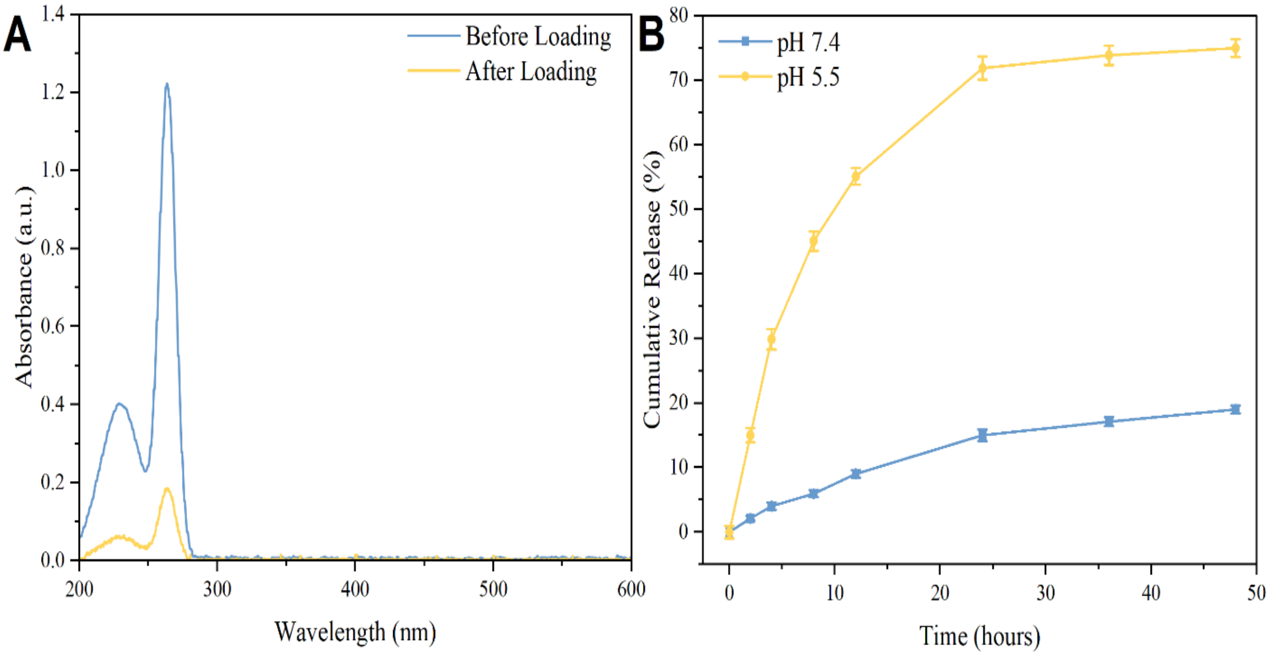

Figure 6. (A) UV-vis absorption spectra of the 5-ALA aqueous solution before and after the loading procedure, used to quantify drug loading. (B) In vitro cumulative release profiles of 5-ALA from ALA@KCC-1-NH_2 nanoparticles in PBS at pH 7.4 (black squares) and pH 5.5 (red circles) over 48 hours

3.5.In Vitro Biocompatibility and Enhanced Photodynamic Detection

The biocompatibility and therapeutic potential of the nanosystem were evaluated in vitro using the HT-29 human colorectal cancer cell line. The cytotoxicity was assessed using the MTT assay, with results presented in Figure 7 and summarized as IC50 values in Table 3. The blank nanocarrier, KCC-1-NH_2, demonstrated excellent biocompatibility, with cell viability remaining above 90% even at high concentrations (200 µg/mL), indicating the intrinsic safety of the fibrous silica platform [49]. In the absence of light irradiation (dark toxicity), both free 5-ALA and the ALA@KCC-1-NH_2 formulation showed minimal impact on cell viability, confirming that the components are non-toxic without photoactivation. However, upon irradiation with 635 nm light, a significant dose-dependent decrease in cell viability was observed for both 5-ALA-containing groups. Critically, the ALA@KCC-1-NH_2 nanoparticles induced substantially greater phototoxicity than free 5-ALA at equivalent concentrations. The calculated IC50 value for ALA@KCC-1-NH_2 under irradiation was 0.45 mM, approximately three times lower than that of free 5-ALA (1.38 mM), demonstrating a markedly enhanced photodynamic effect [50]. In order to benchmark our results, we compiled a literature comparison of 5-ALA delivery systems that report particle size, loading capacity or encapsulation efficiency, pH-responsive release where available, model system, and fluorescence/phototoxicity outcomes. As summarized in Table 4, ALA@KCC-1-NH2 combines high drug loading (15.3 wt%) and encapsulation efficiency (85.6%) with acid-triggered release and stronger phototoxicity on HT-29 cells relative to free 5-ALA, while values reported for liposomes, PLGA nanoparticles, ethosomes, and gold-nanoparticle conjugates fall within lower loading/encapsulation ranges or demonstrate improvements in other models under different conditions. We note that illumination parameters, dosing, and cell lines vary across studies; comparisons are therefore indicative rather than absolute. To mechanistically link enhanced phototoxicity to intracellular photochemistry, we quantified PpIX and ROS dynamics. Quantitative plate-reader assays corroborated confocal findings by revealing steeper PpIX concentration–response and a higher plateau for ALA@KCC-1-NH2 versus free 5-ALA, together with faster accumulation over 0.5–8 h. Upon 635 nm exposure, DCFH-DA readouts showed a larger irradiation-dependent ROS increase for ALA@KCC-1-NH2; NAC reduced these signals as an internal specificity control. PpIX photobleaching, analyzed by normalizing fluorescence to pre-irradiation intensity and fitting mono-exponential decays, proceeded at rates consistent with prior PpIX photophysics; when normalized to initial fluorescence, decay constants were comparable across groups, indicating that higher initial intracellular PpIX—rather than altered bleaching kinetics—predominantly drives the amplified effect. Time- and concentration–response curves for viability (MTT) were fitted to 4-parameter logistic models (IC50 with 95% CI). Two-way ANOVA with FDR correction supported significant treatment and time/concentration effects; we now report partial η^2 for omnibus tests and Cohen's *d* for planned pairwise contrasts alongside adjusted *p*-values. A significant limitation of the current study is the use of a single colorectal cancer cell line (HT-29), which restricts the generalizability of our findings. To address this, future investigations are planned to validate the cancer-specific targeting and safety of the ALA@KCC-1-NH_2 system across a broader panel of cells. This will involve incorporating a non-tumoral colon epithelial cell line, such as NCM460 (Shirasawa et al., 1995), to determine the selectivity index of our nanosystem and confirm its safety toward healthy tissue. Furthermore, we will include additional CRC cell lines, such as SW480, which exhibits a different phenotype and genetic profile from HT-29. Comparing PpIX accumulation and phototoxicity in these cell lines will elucidate whether the enhanced delivery is a robust phenomenon in colorectal cancer and will provide crucial data on the system's efficacy across different tumor subtypes [51].

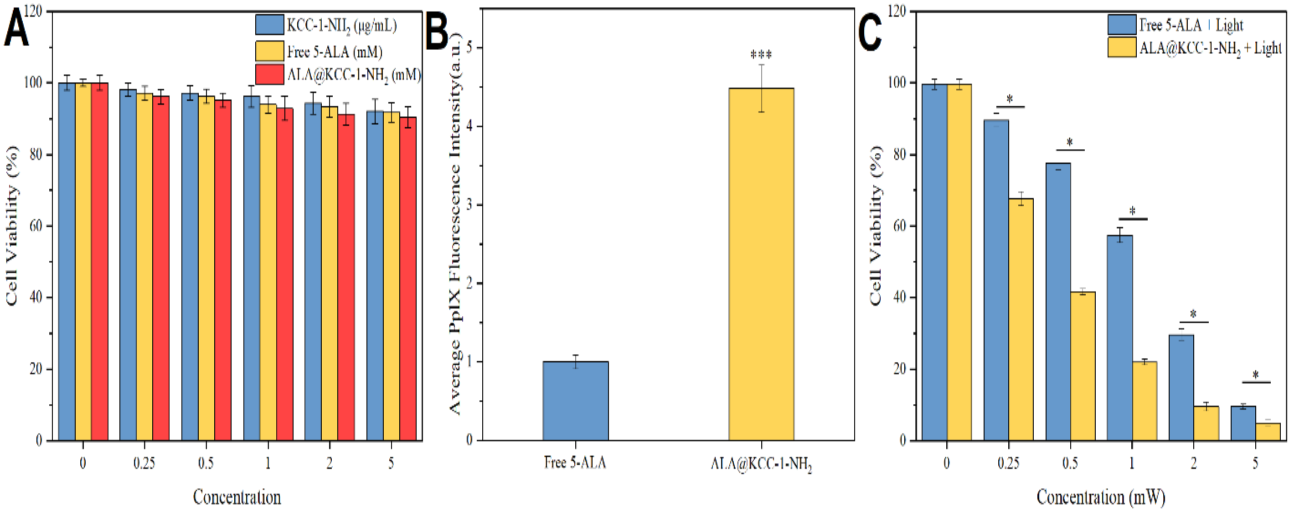

Figure 7. In vitro cytotoxicity of different formulations on HT-29 cells as determined by the MTT assay. (A) Dark toxicity of KCC-1-NH_2, free 5-ALA, and ALA@KCC-1-NH_2. (B) Phototoxicity of free 5-ALA and ALA@KCC-1-NH_2 after irradiation with 635 nm light (20 J/cm²)

Table 3. In Vitro cytotoxicity (IC50 Values) of 5-ALA formulations on HT-29 cells after 48 hours

Formulation	Condition	IC$_{50}$ (mM)
Free 5-ALA	Dark	> 5.0
ALA@KCC-1-NH2	Dark	> 5.0
Free 5-ALA	Light Irradiation (20 J/cm^2)	1.38 ± 0.15
ALA@KCC-1-NH2	Light Irradiation (20 J/cm^2)	0.45 ± 0.08
KCC-1-NH2	Dark	> 200 μg/mL

Table 4. Comparative summary of 5-ALA nano-delivery systems and outcomes

Platform / Carrier	Size (nm)	5-ALA loading / encapsulation	Release behavior (pH)	Model / assay	PpIX fluorescence / phototoxicity outcome	Reference
This work: ALA@KCC-1-NH$_2$ (fibrous nanosilica)	~455 ± 30	DLC 15.3 wt%; EE 85.6%	<20% release @ pH 7.4 (48 h); >70% @ pH 5.5 (24 h)	HT-29; PDT (635 nm, 20 $J\cdot cm^{-2}$)	IC50 0.45 mM (ALA@KCC-1-NH2) vs 1.38 mM (free 5-ALA); confocal CLSM shows stronger intracellular PpIX vs free drug	This study.
DPPC liposomes (5-ALA/DPPC)	84–89	EE ~15–16%	NR	B16F10 melanoma; in vitro/ex vivo	Post-PDT cell viability 33% with liposomes vs 52% with free 5-ALA at equal dosing; enhanced PpIX in ex vivo skin	[52]
PLGA nanoparticles (5ALA@PLGA)	65.6 ± 26	EE 65.8% ± 7.2%; LC 0.62% ± 0.27%	NR	Squamous carcinoma cells; in vitro uptake	Efficient uptake; amorphous ALA in PLGA; PDT efficacy reported vs free drug (conditions differ)	[53]
5-ALA–Au nanoparticle conjugates	NR	NR	NR	Mel-Rm melanoma; PDT in vitro	~2× higher cell death vs free 5-ALA at comparable light doses; higher PpIX induction	[54]
Ethosomes vs liposomes (skin delivery)	<200 (ethosomes)	Ethosome EE 8–66% (surfactant-dependent)	NR	In vivo/ex vivo skin; PpIX visualization	Ethosomes smaller than liposomes; PpIX observed in skin by CLSM	[16]
Baseline (free 5-ALA; no carrier)	—	—	—	HT-29; 1 mM, 4 h	Robust PpIX fluorescence detectable after 4 h in HT-29 and other lines (dose-dependent)	[55]

To elucidate the mechanism behind this enhanced efficacy, the intracellular generation of fluorescent PpIX was visualized using confocal laser scanning microscopy. Figure 8A presents representative fluorescence images of HT-29 cells after a 4-hour incubation with either free 5-ALA or ALA@KCC-1-NH$_2$. The images clearly show that cells treated with the nanoparticle formulation exhibit a dramatically more intense and widespread red fluorescence (indicative of PpIX) throughout the cytoplasm compared to cells treated with free 5-ALA. Quantitative analysis of the fluorescence intensity, shown in Figure 8B, confirms this observation, revealing an approximately 4.5-fold increase in the average PpIX fluorescence signal per cell for the ALA@KCC-1-NH_2 group relative to the free 5-ALA group. Mesoporous silica nanoparticles typically traffic to late endosomes/lysosomes, where the acidic lumen (pH ~4.5–6) and protonation weaken amine–carboxylate interactions, favoring ALA release; this is consistent with the stronger PpIX signal observed for ALA@KCC-1-NH_2. To dissect uptake pathways in future perturbation studies, representative inhibitors can be used (chlorpromazine, clathrin; genistein/filipin, caveolae; EIPA, macropinocytosis), while recognizing documented specificity and toxicity caveats; LysoTracker co-localization should be quantified (Pearson's/Manders') [56,57]. The ~4.5-fold increase in PpIX with ALA@KCC-1-NH_2 is consistent with, but does not by itself prove, enhanced cellular uptake and lysosomal release of 5-ALA. Given literature showing size/charge-dependent endocytic internalization of aminated mesoporous silica and frequent residence in endo/lysosomal compartments, we consider endocytosis-mediated trafficking a plausible route for our system; however, we now present this strictly as a hypothesis to be tested. To that end, we will quantify lysosomal co-localization in HT-29 cells using LysoTracker and rigorous image analysis (Pearson's r and Manders' M1/M2 with Costes thresholding, ≥20 cells/condition), alongside pharmacologic pathway perturbation in follow-up work [58,59]. This increased substrate availability subsequently drives the heme synthesis pathway to produce a greater amount of PpIX, resulting in the observed enhancement in both fluorescence for detection and phototoxicity for therapy [13]. These findings directly validate the central hypothesis of this study and highlight the potential of this fibrous nanosilica platform to significantly improve the sensitivity and efficacy of 5-ALA-based cancer diagnostics and therapeutics. Relative to common channel-type MSNs (MCM-41/SBA-15) and non-silica carriers, the fibrous KCC-1 architecture provided three quantifiable gains. (i) DLC/EE: ALA@KCC-1–NH_2 achieved DLC 14.7–15.3 wt% and EE 85–86%, whereas DPPC liposomes typically afford EE ~15–16% at similar sizes (~85 nm), and PLGA affords high EE yet very low LC for hydrophilic ALA (0.62 ± 0.27%). (ii) Release control: our carrier shows negligible leakage at pH 7.4 (<20%/48 h) and rapid release at pH 5.5 (>70%/24 h), consistent with protonation-weakening of ALA–amine electrostatics. (iii) PpIX enhancement at clinically used red-light fluences: at 635 nm, 20 $J\cdot cm^{-2}$ our platform yielded ~4.5-fold higher intracellular PpIX and a ~3× lower IC_{50} vs free ALA (0.45 vs 1.38 mM). Fluences in the 20–37 $J\cdot cm^{-2}$ range are widely employed for ALA-PDT/PDD, supporting the clinical relevance of our light setting [60]. Mechanistically, KCC-1's radially open fibers increase external accessibility and shorten diffusion pathways compared with the tortuous inner channels of MCM-41/SBA-15, which facilitates high surface binding and endosomal release; comparative studies also report improved dispersion/uptake of KCC-1 vs MCM-41 [61]. For 5-ALA specifically, unmodified MSNs better preserve ALA stability than amine-grafted surfaces; our mildly acidic loading (pH 6.5), rapid dark handling, and short storage minimized dimerization while still exploiting amine–carboxylate interactions to achieve high capacity and pH-triggered release [62].

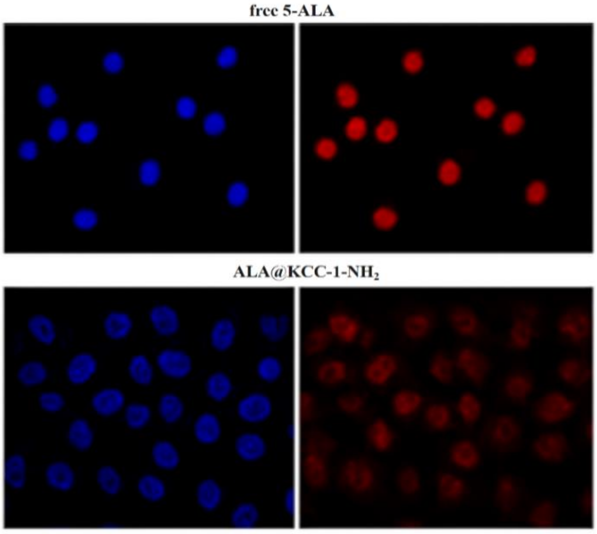

Figure 8. (A) Confocal fluorescence microscopy images of HT-29 cells incubated for 4 hours with free 5-ALA and ALA@KCC-1-NH_2. Blue fluorescence (DAPI) indicates the cell nuclei, and red fluorescence indicates intracellular PpIX. (B) Quantitative analysis of the average intracellular PpIX fluorescence intensity in HT-29 cells treated with free 5-ALA and ALA@KCC-1-NH_2. Data are presented as mean ± SD (n=3). ***$p < 0.001$

4. Conclusion

In this study, we successfully developed and characterized a ALA@KCC-1-NH_2 for enhanced photodynamic applications. The amine-functionalized submicrometre fibrous silica particles (KCC-1; ~455 nm) demonstrated excellent drug-carrying capabilities, achieving a drug loading content of 15.3 wt% and an encapsulation efficiency of 85.6%. The system exhibited a highly desirable pH-responsive release mechanism, remaining stable at physiological pH 7.4 (<20% release at 48 hours) while efficiently liberating its cargo in an acidic endosomal environment (>70% release at pH 5.5 within 24 hours). This controlled delivery translated to superior performance in HT-29 colorectal cancer cells, where the ALA@KCC-1-NH_2 formulation mediated a 4.5-fold increase in intracellular Protoporphyrin IX fluorescence compared to free 5-ALA. Consequently, the nanosystem showed markedly enhanced photodynamic efficacy upon irradiation (635 nm, 20 J/cm²), with an IC_{50} of 0.45 ± 0.08 mM, representing a threefold improvement over free 5-ALA (1.38 ± 0.15 mM). Collectively, these quantitative results establish our fibrous nanosilica platform as a promising candidate for improving 5-ALA-based photodynamic diagnosis, with potential for therapeutic application in colorectal cancer. While this work provides a strong in vitro proof-of-concept, future preclinical validation in ex vivo and in vivo models is essential to determine the system's safety and efficacy before its potential for clinical translation can be fully assessed.

Authors Contributions

All the authors have participated sufficiently in the intellectual content, conception, and design of this work or the analysis and interpretation of the data (when applicable), as well as the writing of the manuscript.

Availability of data and materials

The data that support the findings of this study are available from the corresponding author, upon reasonable request.

Conflict of interest

The author states that there is no conflict of interest.

Reference

[1] T. Namikawa, T. Yatabe, K. Inoue, T. Shuin, K. Hanazaki. “Clinical applications of 5-aminolevulinic acid-mediated fluorescence for gastric cancer”. *World J. Gastroenterol.,* 21, 8769–8775, (2015).

[2] H. Xu, Y. Han, Y. Wu, Y. Wang, Q. Li, P. Zhang, P. Yuan, Y. Luo, Y. Fan, S. Chen, R. Cai, Q. Li, F. Ma, B. Xu, J. Wang. “Clinicopathological characteristics and prognosis of HER2-low early-stage breast cancer: A single-institution experience”. *Front. Oncol.,* 12, 906011, (2022).

[3] I. Maggio, E. Franceschi, A. Tosoni, V. Nunno, L. Gatto, R. Lodi, A. Brandes. “Meningioma: Not always a benign tumor. A review of advances in the treatment of meningiomas”. *CNS Oncol.,* 10, 0003, (2021).

[4] J. Vogel, S. Felder, A. Bhama, A. Hawkins, S. Langenfeld, V. Shaffer, A. Thorsen, M. Weiser, G. Chang, A. Lightner, D. Feingold, I. Paquette. “The American Society of Colon and Rectal Surgeons clinical practice guidelines for the management of colon cancer”. *Dis. Colon Rectum,* 65, 148–177, (2021).

[5] R. Taoka, Y. Matsuoka, M. Yamasaki, N. Kani, T. Honda, S. Harada, Y. Tohi, T. Kato, H. Okazoe, H. Tsunemori, N. Ueda, M. Sugimoto. “Photodynamic diagnosis-assisted transurethral resection using oral 5-aminolevulinic acid decreases residual cancer and improves recurrence-free survival in patients with non-muscle-invasive bladder cancer”. *Photodiagnosis Photodyn. Ther.,* 38, 102838, (2022).

[6] A. Honor, S. Rudnick, H. Bonkovsky. “Givosiran to treat acute porphyria”. *Drugs Today* 57, 47, (2021).

[7] T. Fan, L. Roling, B. Hedtke, B. Grimm. “FC2 stabilizes POR and suppresses ALA formation in the tetrapyrrole biosynthesis pathway”. *New Phytol.,* 239, 624–638, (2023).

[8] M. Miljkovic, A. Seguin, X. Jia, J. Cox, J. Catrow, H. Bergonia, J. Phillips, W. Stephens, D. Ward. “Loss of the mitochondrial protein Abcb10 results in altered arginine metabolism in MEL and K562 cells and nutrient stress signaling through ATF4”. *J. Biol. Chem.,* 299, 104877, (2023).

[9] S. Ebrahimi, M. Ghadiri, W. Stummer, A. Gorji. “Enhancing 5-ALA-PDT efficacy against resistant tumor cells: Strategies and advances”. *Life Sci.,* 351, 122808, (2024).

[10] Y. Harada, Y. Murayama, T. Takamatsu, E. Otsuji, H. Tanaka. “5-Aminolevulinic acid-induced protoporphyrin IX fluorescence imaging for tumor detection: Recent advances and challenges”. *Int. J. Mol. Sci.,* 23, 6478, (2022).

[11] F.R. Abbas Abad, M. Pourmadadi, M. Abdouss, A. Rahdar, S. Fathi-karkan, S. Pandey. “Targeted nanoparticle delivery of lapatinib for cancer therapy: Progress, challenges, and future directions”. *J. Drug Deliv. Sci. Technol.,* 108, 106902, (2025).

[12] M. Pourmadadi, N. Ajalli, M. Nouri, M. Shirazi, M. Hashemipour, N. Hosseini, S. Fathi-karkan, M. Azizi, A. Rahdar, S. Pandey. “Enhanced drug delivery of 5-fluorouracil using a GO-PVP-SA nanocomposite for targeted colorectal cancer treatment”. *BioNanoSci.,* 15, 194, (2025).

[13] Y. Harada, Y. Murayama, T. Takamatsu, E. Otsuji, H. Tanaka. “5-Aminolevulinic acid-induced protoporphyrin IX fluorescence imaging for tumor detection: Recent advances and challenges”. *Int. J. Mol. Sci.,* 23, 6478, (2022).

[14] Y. Gao, D. Gao, J. Shen, Q. Wang. “A review of mesoporous silica nanoparticle delivery systems in chemo-based combination cancer therapies”. *Front. Chem.,* 8, 598722, (2020).

[15] E. Chibowski, A. Szcześ. “Zeta potential and surface charge of DPPC and DOPC liposomes in the presence of PLC enzyme”. *Adsorption,* 22, 755–765, (2016).

[16] Y.-P. Fang, Y.-H. Tsai, P.-C. Wu, Y.-B. Huang. “Comparison of 5-aminolevulinic acid-encapsulated liposome versus ethosome for skin delivery for photodynamic therapy”. *Int. J. Pharm.,* 356, 144–152, (2008).

[17] X. Ma, Q. Qu, Y. Zhao. “Targeted delivery of 5-aminolevulinic acid by multifunctional hollow mesoporous silica nanoparticles for photodynamic skin cancer therapy”. *ACS Appl. Mater. Interfaces,* 7, 10671–10676, (2015).

[18] S. Thepwatee, J. Pramongkit, P. Kimjui. “Controlled release of Mahaad extract using Span 80 co-loaded on a dendritic fibrous silica”. *Mater. Sci. Forum*, 1100, 57–63, (2023).

[19] R. Soltani, R. Pelalak, M. Pishnamazi, A. Marjani, A. Albadarin, S. Sarkar, S. Shirazian. “Synthesis of multi-organo-functionalized fibrous silica KCC-1 for highly efficient adsorption of acid fuchsine and acid orange II from aqueous solution”. *Sci. Rep.*, 11, 81080, (2021).

[20] M. Behyar, N. Shadjou. “d-Penicillamine functionalized dendritic fibrous nanosilica (DFNS-DPA): Synthesis and its application as an innovative advanced nanomaterial towards sensitive quantification of ractopamine”. *RSC Adv.*, 11, 30206–30214, (2021).

[21] Z. Mohammadbagheri and A. Najafi Chermahini. “KCC-1/Pr-SO3H as an efficient heterogeneous catalyst for production of *n*-butyl levulinate from furfuryl alcohol”. *J. Ind. Eng. Chem.* 62, 401–408, (2018).

[22] N. Bayal, B. Singh, R. Singh, and V. Polshettiwar. “Size and fiber density controlled synthesis of fibrous nanosilica spheres (KCC-1)”. *Sci. Rep.*, 6, 24888, (2016).

[23] A. Maity and V. Polshettiwar. “Dendritic fibrous nanosilica for catalysis, energy harvesting, carbon dioxide mitigation, drug delivery, and sensing”. *ChemSusChem*, 10, 3866–3913, (2017).

[24] J. Shabir, S. Rani, M. Sharma, C. Garkoti, Surabhi, and S. Mozumdar. “Synthesis of dendritic fibrous nanosilica over a cubic core (cSiO2@DFNS) with catalytically efficient silver nanoparticles for reduction of nitroarenes and degradation of organic dyes”. *RSC Adv.*, 10, 8140–8151, (2020).

[25] B.G. Trewyn, I.I. Slowing, S. Giri, H.-T. Chen, and V.S.-Y. Lin. “Synthesis and functionalization of a mesoporous silica nanoparticle based on the sol–gel process and applications in controlled release”. *Acc. Chem. Res.*, 40, 846–853, (2007).

[26] R. Fatima, P. Katiyar, and K. Kushwaha. “Recent advances in mesoporous silica nanoparticle: synthesis, drug loading, release mechanisms, and diverse applications”. *Front. Nanotechnol.*, 7:1564188, (2025).

[27] J. Li, Q. Wang, Z. Wang, N. Cui, B. Yang, and W. Niu. “Tetrandrine inhibits colon carcinoma HT-29 cells growth via the Bcl-2/Caspase 3/PARP pathway and G1/S phase”. *Biosci. Rep.*, 39, BSR20182109, (2019).

[28] N. Jirofti, F. Sarhaddi, A. Jahani, A. Rahdar, F. Kalalinia, R.E. Malekshah, Z. Ebrahimnezhad, N. Rahiman, S. Fathi-karkan, P. Taboada, and S. Pandey. “Development and characterization of polymer-stabilized dobutamine nanomicelles for improved drug delivery”. *Nano LIFE*, 16, 2550002, (2026).

[29] E. Yoshioka, V.S. Chelakkot, M. Licursi, S.G. Rutihinda, J. Som, L. Derwish, J.J. King, T. Pongnopparat, K. Mearow, M. Larijani, A.M. Dorward, and K. Hirasawa. “Enhancement of cancer-specific protoporphyrin IX fluorescence by targeting oncogenic Ras/MEK pathway”. *Theranostics*, 8, 2134–2146, (2018).

[30] Z.S. Hoseini, S. Zeinalilathori, S. Fathi-karkan, S. Zeinali, A. Rahdar, B. Siddiqui, Z. Kharaba, and S. Pandey. “Cell-targeting nanomedicine for bladder cancer: A cellular bioengineering approach for precise drug delivery”. *J. Drug Deliv. Sci. Technol.*, 101, 106220, (2024).

[31] Y. Wang, K. Hu, J. He, and Y. Zhang. “Improving the size uniformity of dendritic fibrous nano-silica by a facile one-pot rotating hydrothermal approach”. *RSC Adv.*, 9, 24783–24790, (2019).

[32] H. Cabral, Y. Matsumoto, K. Mizuno, Q. Chen, M. Murakami, M. Kimura, Y. Terada, M.R. Kano, K. Miyazono, M. Uesaka, N. Nishiyama, and K. Kataoka. “Accumulation of sub-100 nm polymeric micelles in poorly permeable tumours depends on size”. *Nat. Nanotechnol.*, 6, 815–823, (2011).

[33] L. Tang, X. Yang, Q. Yin, K. Cai, H. Wang, I. Chaudhury, C. Yao, Q. Zhou, M. Kwon, J.A. Hartman, I.T. Dobrucki, L.W. Dobrucki, L.B. Borst, S. Lezmi, W.G. Helferich, A.L. Ferguson, T.M. Fan, and J. Cheng. “Investigating the optimal size of anticancer nanomedicine”. *Proc. Natl. Acad. Sci. U.S.A.*, 111, 15344–15349, (2014).

[34] A. Fihri, D. Cha, M. Bouhrara, N. Almana, and V. Polshettiwar. “Fibrous nano-silica (KCC-1)-supported palladium catalyst: Suzuki coupling reactions under sustainable conditions”. *ChemSusChem*, 5, 85–89, (2012).

[35] H. Liang, Z. Cao, C. Xia, F. Ming, W. Zhang, A. Emwas, L. Cavallo, and H. Alshareef. “Tungsten blue oxide as a reusable electrocatalyst for acidic water oxidation by plasma-induced vacancy engineering”. *CCS Chem.*, 3, 1553–1561, (2020).

[36] Y. Li, J. Xie, and D. Cao. “In situ silver nanoparticle–hyaluronic acid hydrogel for enhanced wound healing”. *J. Nanostruct. Chem.* 15:152516, (2025).

[37] D. Mohammadi, A.H. Aghayan, D. Mohammadi, M.J. Mashhadi, Z. Jamalpoor, A. Rahdar, and S. Pandey. “Therapeutic effects of silibinin on animal models of skin cancer: A systematic review and meta-analysis”. *BioNanoSci.*, 15, 414, (2025).

[38] J. Sun, Z. Xu, W. Li, and X. Shen. “Effect of nano-SiO_2 on the early hydration of alite-sulphoaluminate cement”. *Nanomaterials*, 7, 102, (2017).

[39] L. Wang, A. Lu, C. Wang, X. Zheng, and D. Zhao. “Nano-fibriform production of silica from natural chrysotile”. *J. Colloid Interface Sci.*, 295, 436–439, (2006).

[40] I. Miletto, E. Bottinelli, A. Siviero, D. Fabbri, P. Calza, and G. Berlier. “Mesoporous nanocarriers for the loading and stabilization of 5-aminolevulinic acid”. *J. Nanopart. Res.*, 18, 227, (2016).

[41] M. Shirzad, A. Salahvarzi, S. Fathi-karkan, A. Rahdar, M. Guettari, and S. Pandey. “Green nanocarriers and biodegradable systems for sustainable drug delivery solutions”. *J. Drug Deliv. Sci., Technol.* 111, 107208, (2025).

[42] M. Mahmoudian, M.A. Gharabaghlou, and N. Shadjou. “Utilization of a mixed matrix membrane modified by novel dendritic fibrous nanosilica (KCC-1-NH-CS2) toward water purification”. *RSC Adv.*, 12, 17514–17526, (2022).

[43] I. Miletto, E. Bottinelli, A. Siviero, D. Fabbri, P. Calza, and G. Berlier. “Mesoporous nanocarriers for the loading and stabilization of 5-aminolevulinic acid”. *J. Nanopart. Res.*, 18, 227, (2016).

[44] K. Choi, S. Lee, J.O. Park, J.-A. Park, S.-H. Cho, S.Y. Lee, J.H. Lee, and J.-W. Choi. “Chromium removal from aqueous solution by a PEI-silica nanocomposite”. *Sci. Rep.* 8, 1438, (2018).

[45] A. Marjani and R.K. Mohammadi. “Synthesis of novel adsorbent based on tetrasulfide-functionalized fibrous silica KCC-1 for removal of Hg(II) cations”. *Sci. Rep.*, 11, 10735, (2021).

[46] Z. Mohammadi, A. Sazgarnia, O. Rajabi, S. Soudmand, H. Esmaily, and H.R. Sadeghi. “An in vitro study on the photosensitivity of 5-aminolevulinic acid conjugated gold nanoparticles”. *Photodiagn. Photodyn. Ther.*, 10, 382–388, (2013).

[47] G. Giovaninni, C.J. Moore, A.J. Hall, H.J. Byrne, and V. Gubala. “pH-dependent silica nanoparticle dissolution and cargo release”. *Colloids Surf. B Biointerfaces*, 169, 242–248, (2018).

[48] S. B. Tian, B. Huo, H. Liu, Y. Zhang, and X. Li. “Development of a biocompatible PLGA-based nanoplatform for targeted delivery of empagliflozin and enhanced cytotoxicity against gastric carcinoma cells”. *J. Nanostruct. Chem.*, 15, 152514, (2025).

[49] W. Lin, Y. Huang, X.-D. Zhou, and Y. Ma. “In vitro toxicity of silica nanoparticles in human lung cancer cells”. *Toxicol. Appl. Pharmacol.*, 217, 252–259, (2006).

[50] X. Ma, Q. Qu, and Y. Zhao. “Targeted delivery of 5-aminolevulinic acid by multifunctional hollow mesoporous silica nanoparticles for

photodynamic skin cancer therapy”. *ACS Appl. Mater. Interfaces,* 7, 10671–10676, (2015).

[51] S. Shirasawa, M. Furuse, N. Yokoyama, and T. Sasazuki. “Altered growth of human colon cancer cell lines disrupted at activated Ki-ras”. *Science,* 260, 85–88, (1993).

[52] M.-W. Lin, Y.-B. Huang, C.-L. Chen, P.-C. Wu, C.-Y. Chou, P.-C. Wu, and S.-Y. Hung. “A formulation study of 5-aminolevulinic encapsulated in DPPC liposomes in melanoma treatment”. *Int. J. Med. Sci.,* 13, 483–489, (2016).

[53] L. Shi, X. Wang, F. Zhao, H. Luan, Q. Tu, Z. Huang, and H. Wang. “In vitro evaluation of 5-aminolevulinic acid (ALA) loaded PLGA nanoparticles”. *Int. J. Nanomedicine* 8, 2669–2676, (2013).

[54] Z. Mohammadi, A. Sazgarnia, O. Rajabi, S. Soudmand, H. Esmaily, and H.R. Sadeghi. “An in vitro study on the photosensitivity of 5-aminolevulinic acid conjugated gold nanoparticles”. *Photodiagn. Photodyn. Ther.,* 10, 382–388, (2013).

[55] Y. Kitajima, T. Ishii, T. Kohda, M. Ishizuka, K. Yamazaki, Y. Nishimura, T. Tanaka, S. Dan, and M. Nakajima. “Mechanistic study of PpIX accumulation using the JFCR39 cell panel revealed a role for dynamin 2-mediated exocytosis”. *Sci. Rep.,* 9, 8666, (2019).

[56] I. Schütz, T. Lopez-Hernandez, Q. Gao, D. Puchkov, S. Jabs, D. Nordmeyer, M. Schmudde, E. Rühl, C.M. Graf, and V. Haucke. “Lysosomal dysfunction caused by cellular accumulation of silica nanoparticles”. *J. Biol. Chem.,* 291, 14170–14184, (2016).

[57] G. Giovaninni, C.J. Moore, A.J. Hall, H.J. Byrne, and V. Gubala. “pH-dependent silica nanoparticle dissolution and cargo release”. *Colloids Surf. B Biointerfaces,* 169, 242–248, (2018).

[58] J. Sun, Y. Liu, M. Ge, G. Zhou, W. Sun, D. Liu, X.-J. Liang, and J. Zhang. “A distinct endocytic mechanism of functionalized-silica nanoparticles in breast cancer stem cells”. *Sci. Rep.,* 7, 16236, (2017).

[59] M. Ekkapongpisit, A. Giovia, C. Follo, G. Caputo, and C. Isidoro. “Biocompatibility, endocytosis, and intracellular trafficking of mesoporous silica and polystyrene nanoparticles in ovarian cancer cells: Effects of size and surface charge groups”. *Int. J. Nanomedicine,* 7, 4147–4158, (2012).

[60] K. Wojewoda, M. Gillstedt, J. Tovi, L. Salah, A.-M. Wennberg Larkö, A. Sjöholm, and C. Sandberg. “Optimizing treatment of acne with photodynamic therapy (PDT) to achieve long-term remission and reduce side effects: A prospective randomized controlled trial”. *J. Photochem. Photobiol. B Biol.,* 223, 112299, (2021).

[61] B. Singh and V. Polshettiwar. “Design of CO2 sorbents using functionalized fibrous nanosilica (KCC-1): Insights into the effect of the silica morphology (KCC-1 vs. MCM-41)”. *J. Mater. Chem. A,* 4, 7005–7019, (2016).

[62] I. Miletto, E. Bottinelli, A. Siviero, D. Fabbri, P. Calza, and G. Berlier. “Mesoporous nanocarriers for the loading and stabilization of 5-aminolevulinic acid”. *J. Nanopart. Res.,* 18, 227, (2016).